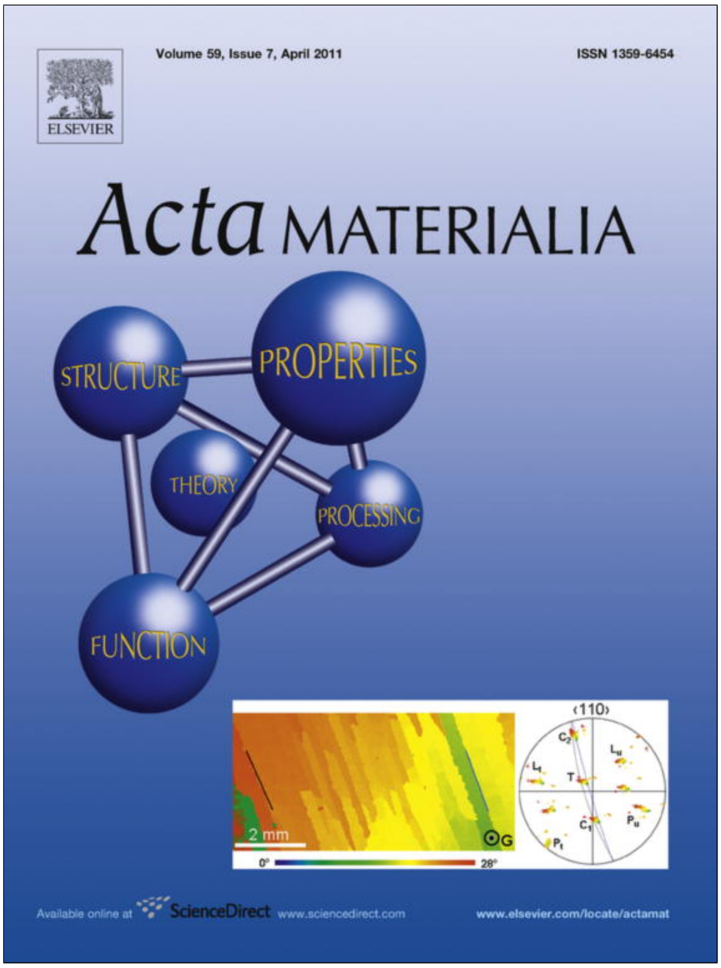
Volume 59, Issue 7, April 2011
ISSN 1359-6454
ELSEVIER
Acta MATERIALIA
STRUCTURE
PROPERTIES
THEORY
PROCESSING
FUNCTION
Available online at ScienceDirect www.sciencedirect.com
www.elsevier.com/locate/actamat

Available online at www.sciencedirect.com

ScienceDirect

Acta Materialia 59 (2011) 2624–2636

Acta MATERIALIA

www.elsevier.com/locate/actamat

Topology optimization for negative permeability metamaterials using level-set algorithm

Shiwei Zhou, Wei Li, Yuhang Chen, Guangyong Sun, Qing Li *

School of Aerospace, Mechanical and Mechatronic Engineering, The University of Sydney, Sydney, NSW 2006, Australia

Received 1 June 2010; received in revised form 25 December 2010; accepted 27 December 2010
Available online 4 February 2011

Abstract

This paper aims to develop a level-set-based topology optimization approach for the design of negative permeability electromagnetic metamaterials, where the topological configuration of the base cell is represented by the zero-level contour of a higher-dimensional level-set function. Such an implicit expression enables us to create a distinct interface between the free space and conducting phase (metal). By seeking for an optimality of a Lagrangian functional in terms of the objective function and the governing wave equation, we derived an adjoint system. The normal velocity (sensitivity) of the level-set model is determined by making the Eulerian derivative of the Lagrangian functional non-positive. Both the governing and adjoint systems are solved by a powerful finite-difference time-domain algorithm. The solution to the adjoint system is separated into two parts, namely the self-adjoint part, which is linearly proportional to the solution of the governing equation; and the non-self-adjoint part, which is obtained by swapping the locations of the incident wave and the receiving planes in the simulation model. From the demonstrative examples, we found that the well-known U-shaped metamaterials might not be the best in terms of the minimal value of the imaginary part of the effective permeability. Following the present topology optimization procedure, some novel structures with desired negative permeability at the specified frequency are obtained.

Keywords: Metamaterial; Negative permeability; Negative refractive index; Level-set method; Topology optimization

1. Introduction

Metamaterials signify a new and special class of artificial periodical structures fabricated in a micro- or even nano-scale to obtain such extraordinary electromagnetic properties as negative permeability and/or negative permittivity at megahertz or optical frequency. The theoretical framework was proposed by Veselago [1] as early as the 1960s, but had not attracted much attention due to the inexistence of such materials until recently. After long-time research for the media with sophisticatedly shaped inclusions (e.g. ω-like shape in Ref. [2]), a novel composite with bi-helix-shaped conducting inclusion was devised by Lagarkov in 1997, which was found to have negative permeability experimentally [3]. Two years later, Pendry et al. [4] numerically demonstrated that a non-magnetic conducting microstructure with double split ring resonators (SSRs) has negative permeability. Subsequently, Smith et al. [5] devised a composite medium with both negative permeability and negative permittivity concurrently by assembling a periodic array of interspaced SRRs and continuous wires. Their pioneering work has paved a new avenue to control electromagnetic waves at will, thereby making some equipment which was thought to exist only in myths, such as an invisible cloak [6] and a super lens [7], physically possible.

The reason why metamaterials have such unusual properties is due to the electromagnetic resonances induced in some specially designed structures over a spectrum of frequencies. In addition to the SRR structures, many other special structures (e.g. U-shaped, S-shaped and complex-shaped base cell) were proposed and tested in different frequency ranges [8–10]. The roles of these novel structures in achieving desired functional performance and facilitating

* Corresponding author. Tel.: +61 2 9351 8607; fax: +61 2 9351 7060.
E-mail address: Qing.Li@Sydney.edu.au (Q. Li).

1359-6454/$36.00 © 2010 Acta Materialia Inc. Published by Elsevier Ltd. All rights reserved.
doi:10.1016/j.actamat.2010.12.049

fabrication are evident. For example, the layered U-shaped structures allow the generation of a certain level of negative permeability and is fairly easy to be fabricated in nano-scale for its relatively simple geometry [9]. In order to cancel out the resonant responses to the magnetic field but keep those to the electric field, some simple structures with uniaxial or biaxial symmetry layouts were also proposed, as in Ref. [10]. Nevertheless, all the above-mentioned structures are devised empirically and such a trial-and-error approach appears less efficient when seeking for some specified or extremized electromagnetic properties under more complicated conditions.

Being aware of the challenges, some researchers attempted to introduce various optimization techniques into metamaterial design recently. By optimally distributing the void and conducting materials into the hexagon pixels, several magnetic and electric structures attaining the target negative permeability/permittivity and negative refractive index were obtained by using a non-gradient genetic algorithm (GA), demonstrating the versatility and applicability of optimization methods [11]. With the solid isotropic material with penalization (SIMP) method [12,13] that has been widely used in structural topology optimization, several metamaterials with negative permeability were designed by materializing the local elements with metal phase or free space in the finite element framework [14]. In the SIMP method, the sensitivity of the objective function with respect to the design variables were derived by a two-step adjoint variable method [15] and was applied to a gradient-based optimizer (namely, method of moving asymptotes – MMA [16]) such that the objective function can be minimized. Based upon an increasing popularity of the level-set technique [17] and its special features in a range of fields [18–29], we attempted to develop a level-set-based topology optimization algorithm for the electromagnetic metamaterial design in our previous study, where some benchmark topologies were regenerated in a systematic way. The level-set algorithm demonstrated several noticeable advantages, e.g. more smoothly capturing interfacial evolution and better accommodating an adaptive mesh [26]. Nevertheless, our early work [25] was based on an intuitive observation on a series of existing metamaterial designs and was aimed to generate a desirable loop of current flow on the metal surface for generating resonance, where the objective function was not explicitly related to the effective electromagnetic properties. Also the process was governed by the electric field integral equation (EFIE) and solved by the method of moment (MoM) [30] in an adaptive triangular mesh rather than by Maxwell's equations in the typical rectangular elements. Overall, in spite of such above-mentioned attempts, the topology optimization for metamaterials is still in its infancy and substantial work is needed to make it more versatile and effective in accommodating various specific design issues.

Compared with the density-based topology methods that represent the structural configuration in a point or piecewise fashion, the level-set method continuously captures the structural boundaries, which can be rather critical to such complicated problems as electromagnetic metamaterial design. With a given normal velocity, the boundaries can be driven smoothly. In such an evolution process, the topological variation of the structure can take place in a more natural fashion whilst the objective function is minimized. Due to these features, the level-set technique has been widely used in a range of engineering problems [18–26]. In the electromagnetic fields, one of the most prevalent applications of the level-set method is perhaps in the nonlinear inverse problem [31], where the shape of an unknown object can be reconstructed by minimizing the difference between the electromagnetic fields scattered from the real and the in-design objects. As this technique allows seeing through the non-transparent objects, its engineering value seems tremendous. Such success showed a great potential to extend the level-set method to other electromagnetic design [32,33].

The key to metamaterial design lies in constructing a well-defined structural configuration so that the electromagnetic resonance can be induced and manipulated. From the topology optimization point of view [34], an objective function that is used to measure the metamaterial performance should be minimized by materializing the design domain (base cell) in either metal or free space properly. In this paper, the objective functions are formulated directly in terms of the effective permeability or the least square of the difference between the effective values and their targets. It is noted that the objective functions for metamaterial design appear to be rather sensitive to the shape and topological change. We found that the objective function can fluctuate drastically with the breakage of the local connectivity in some critical elements [25]. Some numerical tests even show that the effective permeability can jump from negative to positive territory with only one element changed. Thus, it is important to capture the geometrical details of the metamaterials by using a proper mesh size.

In this paper, we adopted a more efficient and widely accepted algorithm in electromagnetics context, namely the finite-difference time-domain (FDTD) method [35], to solve both the governing equation, namely the vector wave equation (one type of the Maxwell's equations), and its adjoint system. This method enables us to discretize the base cell domain to a mesh size up to $ny \times nz = 64 \times 64$ in a general personal computer. For the adjoint system, its solution is separated into two parts: (1) the self-adjoint part that is linearly proportional to the solution of the governing equation, and (2) the non-self-adjoint part that is obtained by swapping the locations of the incident wave and the receiving planes in the numerical model. In this paper, the adjoint system is derived from the optimality condition of the Lagrangian functional in terms of the summation of the objective function and the governing equations at a saddle point. By making the Eulerian derivative of the Lagrangian functional non-positive, the normal velocity of the level-set method can be defined. In this paper, we will show that starting from a number of randomly distributed (but vertically symmetric) circular spots the level-set method allows optimizing the size, shape and topology concurrently. In addition to the U-shaped configuration, several novel structures which attain the target or minimal permeability are obtained through the optimization.

Following this introduction, Section 2 defines the model for metamaterial design and extracts the effective properties. Section 3 elucidates the level-set technique for metamaterial design and derives the normal velocity to minimize the objective function. Section 4 presents a number of demonstrative examples based on the present level-set topology optimization method. Finally, Section 5 draws some conclusions.

2. Statement of the problem

In this section, we first set up a numerical model, aiming to obtain the reflection and transmission coefficients that are the basic parameters used to extract the effective electromagnetic properties for metamaterial design. Furthermore, the Maxwell's equations are simplified to a waveguide discontinuity model to facilitate the sensitivity analysis in Section 3.

2.1. Simulation model

Metamaterials have been typically designed as a class of composites constructed by periodically ranked base cells (Fig. 1a). Since the electromagnetic properties of metamaterials can be extracted from the base cell in Fig. 1b, we would like to focus on this representative element. It is noted that the extraordinary properties of metamaterials come from the electromagnetic resonance when the incident wave impinges on the metal surface [1,4,5]. This process can be illustrated in Fig. 1 as follows: (1) the design domain governed by the Maxwell's equations is a cube with 50 μm in the side length; (2) the metal (gold) structure is printed within a 36 × 36 μm square base cell (dashed square in Fig. 2) centrally located at the 50 × 50 μm substrate made by semi-insulating gallium arsenide (GaAs); (3) the metal surface is located at the y–z plane that is parallel to the electric field **E** but perpendicular to the magnetic field **H**; (4) a beam of incident wave is applied to the cube on surface S_1 and propagates along the z direction, namely the direction of Poynting vector **k**; (5) this wave is transmitted to surface S_2 and reflected back to S_1. Such a model has been validated experimentally and numerically in literature [10]. This model implies that such a metamaterial design can be modeled in a 2.5-dimensional optimization problem, in which the base cell is optimized in two dimensions while the Maxwell's equations are solved in three-dimensional space.

To study the effective properties of metamaterial, the conducting material in the base cell is regarded as an obstacle in the waveguide. In two-dimensional space, as shown in Fig. 2, the cross-section of the cube defines a square with $a = 50$ μm in width. The incident electric field $\mathbf{E}^{\mathbf{I}} = E_0\mathbf{y}\exp^{-jk_0z_1}$ is applied to S_1 ($z_1 = -25$ μm) and received at S_2 ($z_2 = 25$ μm), where the magnitude of the electric field is denoted as E_0 and $\mathbf{y} = [0\ 1\ 0]^T$ is a unit vector parallel to the direction of the incident electric field. To make the electric field be a summation of the incident and reflected fields at S_1, the incident and receiving surfaces S_1 and S_2 should be placed far enough from the boundaries of base cell [36]. In this model, the reflection coefficient S_{11} and transmission coefficient S_{21} are defined in terms of the distribution of the electric field and the incident electric field over these two surfaces S_1 and S_2, mathematically given by [36]

$$S_{11} = \frac{2\exp^{-jk_0z_1}}{a^2E_0}\int_{S_1}\mathbf{E}\cdot\mathbf{y}\,dS - 2\exp^{-2jk_0z_1} \tag{1}$$

$$S_{21} = \frac{2\exp^{jk_0z_2}}{a^2E_0}\int_{S2}\mathbf{E}\cdot\mathbf{y}\,dS \tag{2}$$

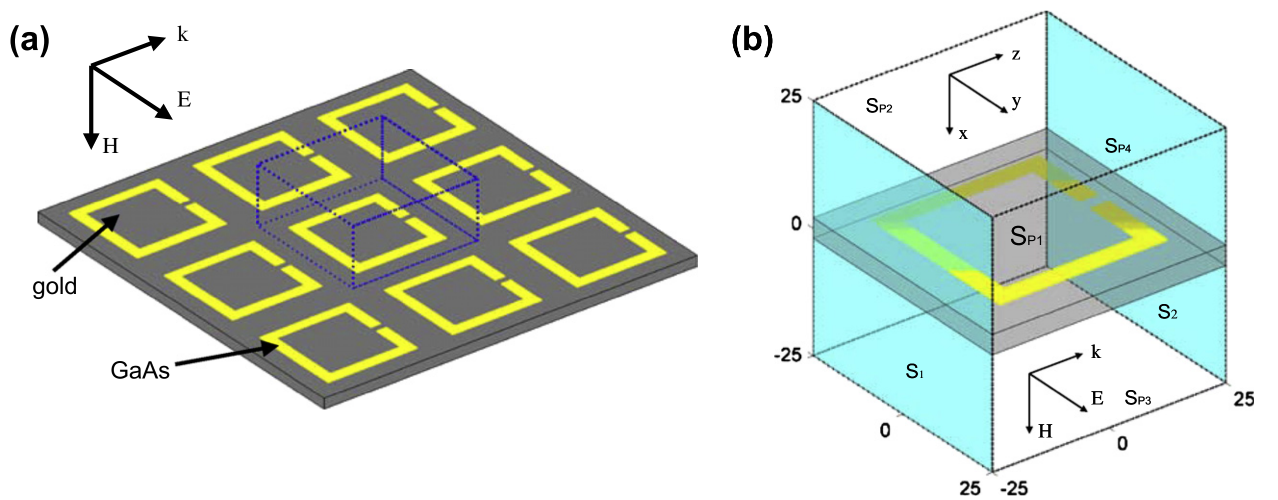

Fig. 1. The schematic of a traditional metamaterial: (a) constructed by periodically ranked base cells on the substrate; (b) the simulation model for the base cell.

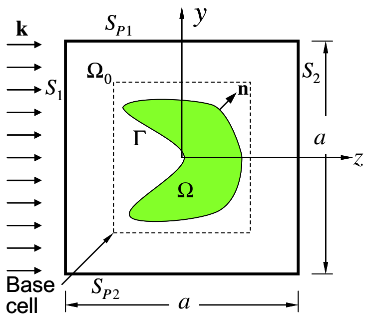

Fig. 2. The schematic of the cross-section of the waveguide discontinuities model.

For convenience of expression, the coefficients are usually expressed in a logarithmic scale (i.e. decibel or dB), as $S_{11} = 20\log_{10} S_{11}$ and $S_{21} = 20\log_{10} S_{21}$.

2.2. The waveguide discontinuities model

The governing Maxwell's equations in the aforementioned model can be simplified to a vector wave equation in terms of electric field $\mathbf{E}$ only, given by

$$\nabla \times (\nabla \times \mathbf{E}) - k_0^2\mathbf{E} = 0 \quad \forall\, \mathbf{x} \in \Omega_0/\Omega \tag{3a}$$

$$\nabla \times (1/\mu_r(\mathbf{x})\nabla \times \mathbf{E}) - (k_0^2\varepsilon_r(\mathbf{x}) - j\sigma(\mathbf{x})\omega\mu_0)\mathbf{E} = 0 \quad \forall\, \mathbf{x} \in \Omega_0 \tag{3b}$$

where domain Ω_0 is a square with width a (Fig. 2). Boundary $\partial\Omega_0$ represents the summation of six surfaces, namely $\partial\Omega_0 = S_1 \cup S_2 \cup S_{p1} \cup S_{p2} \cup S_{p3} \cup S_{p4}$ (Fig. 1). The relative permeability and permittivity of the gold at position $\mathbf{x}$ with respect to the free space are denoted as μ_r and ε_r, respectively. The surface current flow will be induced on gold material as it has a relatively high electrical conductivity σ. The wave number in free space is $k_0 = \omega\sqrt{\mu_0\varepsilon_0} = 2\pi/\lambda_0$, in which ω and λ_0 refer to the frequency and wavelength of the incident wave. The permeability and permittivity of free space are denoted as μ_0 and ε_0. For conciseness of expression, the dependence of the properties of materials on position $\mathbf{x}$ is hidden in the following equations. The continuity condition on free space/metal interface for the electric field is

$$\mathbf{n} \times \mathbf{E}_{in} = \mathbf{n} \times \mathbf{E}_{out} \quad \forall\, \mathbf{x} \in \Gamma \tag{4}$$

$$\varepsilon_r\mathbf{n} \cdot \mathbf{E}_{in} = \mathbf{n} \cdot \mathbf{E}_{out} + \rho_s \quad \forall\, \mathbf{x} \in \Gamma \tag{5}$$

where $\mathbf{n}$ is a unit vector normal on interface Γ and ρ_s is surface charge density. The electric fields inside or outside the metal object but infinitely close to the interface Γ are denoted as $\mathbf{E}_{in}$ or $\mathbf{E}_{out}$, respectively. The boundary conditions are $\mathbf{n}_i \times \mathbf{E} = 0$ and $\mathbf{n}_i \times (\nabla \times \mathbf{E}) = 0$ on the two sets of opposite surfaces ($S_{P1\text{–}2}$ and $S_{P3\text{–}4}$) of the cube, where $\mathbf{n}_i$ ($i = 1, 2, 3, 4$) are the normal vectors to these surfaces. Note that these boundaries act as a perfect electric conductor and a perfect magnetic conductor, which can reasonably reflect the periodicity for the metamaterials [37].

2.3. Effective properties

It is well-known that the effective permeability μ_{eff} depends on the effective impedance z_{eff} and effective refractive index n_{eff} as

$$\mu_{eff} = n_{eff}z_{eff} \tag{6}$$

Based on the model proposed by Lubkowski et al. [38] for the homogeneous metamaterial slab with width d, the relations of the reflection coefficient (S_{11}) and transmission coefficient (S_{21}) to the effective impedance and effective refractive index are defined as

$$S_{11} = (z_{eff} - z_0)/(z_{eff} + z_0) \tag{7}$$

$$S_{21} = \exp^{(-j\omega n_{eff}d/c)} \tag{8}$$

where $c = \sqrt{1/\mu_0\varepsilon_0}$ and $z_0 = \sqrt{\mu_0/\varepsilon_0}$ are the velocity of light and the impedance in free space ($j = \sqrt{-1}$), respectively. The effective permeability depends on the integrals of electric field at the incident and receiving surfaces after substituting Eqs. (7) and (8) into Eq. (6), given by

$$\mu_{eff} = \frac{1+R}{1-R}\frac{jc}{\omega d}\log^{T} \tag{9}$$

where

$$R = \frac{1}{2S_{11}}\left(1 + S_{11}^2 - S_{21}^2 - \sqrt{1 - 2S_{11}^2 - 2S_{11}^2S_{21}^2 + S_{11}^4 - 2S_{21}^2 + S_{21}^4}\right) \tag{10}$$

$$T = \frac{1}{2S_{21}}\left(1 - S_{11}^2 + S_{21}^2 + \sqrt{1 - 2S_{11}^2 - 2S_{21}^2S_{11}^2 + S_{11}^4 - 2S_{21}^2 + S_{21}^4}\right) \tag{11}$$

In addition to this extraction method, other effective retrieval approaches, e.g. Ref. [39], are also applicable. Nevertheless, the above-mentioned method appears more favorable as it suppresses some numerical problems raised from other extraction methods, and more importantly, it is applicable to both the single and double negative metamaterials [38].

3. Level-set model and sensitivity analysis

This section first reviews the classical level-set model proposed by Osher and Sethian [17] in 1988 and then depicts its specific form for the application in metamaterial design. In this paper, the normal velocity of the level-set model is obtained by a sensitivity analysis of the objective function with respect to time through solving an adjoint system. Note that the FDTD method is used herein to solve both the governing and adjoint equations.

3.1. Level-set model and relevant numerical issues

In the level-set model, the profile of a structure is implicitly expressed by the zero-level contour of a higher-dimensional scalar function $\varphi(\mathbf{x})$. Mathematically, the level-set function should be Lipschitz-continuous. As illustrated in

Fig. 3, the negative, zero and positive values of the level-set function separate the design domain into three territories as below:

$$\varphi(\mathbf{x}) < 0 \quad \forall\, \mathbf{x} \in \Omega \tag{12a}$$
$$\varphi(\mathbf{x}) = 0 \quad \forall\, \mathbf{x} \in \Gamma \tag{12b}$$
$$\varphi(\mathbf{x}) > 0 \quad \text{otherwise} \tag{12c}$$

One of the main features of the level-set model is that a complex shape can be embedded in a moving surface governed by the well-known Hamilton–Jacobi (HJ) equation:

$$\frac{\partial \varphi}{\partial t} + V_n \|\nabla \varphi\| = 0 \tag{13}$$

where $\|\nabla\varphi\|$ is the norm of the gradient of the level-set function φ and the normal velocity V_n will be derived from the subsequent sensitivity analysis.

From the level-set model, the vector waveguide equation in Eq. (3) is expressed as

$$\chi_\mu(\varphi,\mu_r)\nabla\times\nabla\times\mathbf{E} - \left(k_0^2\chi_\varepsilon(\varphi,\varepsilon_r) - j\omega\mu_0\chi_\sigma(\varphi,\sigma)\right)\mathbf{E} = 0 \quad \forall\, \mathbf{x} \in \Omega_0 \tag{14}$$

where the characteristic functions χ_μ, χ_ε and χ_σ depend on φ and the local electromagnetic properties as

$$\chi_\mu(\varphi,\mu_r) = H(\varphi) + (1 - H(\varphi))/\mu_r \tag{15a}$$
$$\chi_\varepsilon(\varphi,\varepsilon_r) = H(\varphi) + (1 - H(\varphi))\varepsilon_r \tag{15b}$$
$$\chi_\sigma(\varphi,\sigma) = (1 - H(\varphi))(1+\sigma) + H(\varphi) - 1 \tag{15c}$$

The Heaviside function $H(\varphi)$ is defined as

$$H(\varphi) = \begin{cases} 0 & \varphi < 0 \\ 1 & \varphi > 0 \end{cases} \tag{16}$$

Since the Heaviside function jumps from 0 to 1 discontinuously at $\varphi = 0$, it could result in singularity in numerical implementation. Thus an approximation function that allows varying the change continuously from 0 to 1 within a bandwidth of 2η is used in all the examples below, as

$$H(\varphi) = \begin{cases} 0 & \varphi < -\eta \\ (1 + \varphi/\eta + \sin(\pi\varphi/\eta)/\pi)/2 & \text{otherwise} \\ 1 & \varphi > \eta \end{cases} \tag{17}$$

By multiplying Eq. (14) with a test function $\mathbf{v}$ in the vector-valued Sobolev space on both sides and applying the first vector Green's theorem $\langle \mathbf{a}, \nabla\times\nabla\times\mathbf{b}\rangle_{\Omega_0} = \langle\nabla\times\mathbf{a},\nabla\times\mathbf{b}\rangle_{\Omega_0} - \langle \mathbf{a}\times\nabla\times\mathbf{b},\mathbf{n}\rangle_{\partial\Omega_0}$, its weak form can be obtained as

$$a(\mathbf{E},\mathbf{v}) - \langle\chi_\mu\mathbf{v}\times\nabla\times\mathbf{E},\mathbf{n}\rangle_{\partial\Omega_0} = 0 \tag{18}$$

where $a(\mathbf{E},\mathbf{v}) = \langle\chi_\mu\nabla\times\mathbf{E},\nabla\times\mathbf{v}\rangle_{\Omega_0} - \langle(k_0^2\chi_\varepsilon - j\omega\mu_0\chi_\sigma)\mathbf{E},\mathbf{v}\rangle_{\Omega_0}$ and $\langle\mathbf{a},\mathbf{b}\rangle_{\Omega_0} = \int_{\Omega_0}\mathbf{a}\cdot\mathbf{b}\,d\Omega$ denotes an inner product. Because of the periodic boundary conditions on the walls ($S_{\mathrm{P1-2}}$ and $S_{\mathrm{P3-4}}$), the electric fields on these two sets of opposite surfaces are identical but have opposite normal directions, thus the surface integrals are cancelled out on these boundaries and Eq. (18) becomes

$$a(\mathbf{E},\mathbf{v}) - \langle\chi_\mu\mathbf{v}\times\nabla\times\mathbf{E},\mathbf{n}\rangle_{S_1\cup S_2} = 0 \tag{19}$$

Note that the characteristic function χ_μ can be dropped because $\chi_\mu = 1$ on surfaces S_1 and S_2, the relationship becomes
$\langle\mathbf{a}\times\nabla\times\mathbf{b},\mathbf{n}\rangle_{\partial\Omega_0} = \langle\nabla\times\mathbf{b},\mathbf{n}\times\mathbf{a}\rangle_{\partial\Omega_0} = -\langle\mathbf{a},\mathbf{n}\times\nabla\times\mathbf{b}\rangle_{\partial\Omega_0}$
and the boundary conditions are

$$\mathbf{n}\times\nabla\times\mathbf{E} + jk_0\mathbf{n}\times(\mathbf{n}\times\mathbf{E}) = -2jk_0\mathbf{E}^{\mathbf{I}} \quad \forall\, \mathbf{x} \in S_1 \tag{20a}$$
$$\mathbf{n}\times\nabla\times\mathbf{E} + jk_0\mathbf{n}\times(\mathbf{n}\times\mathbf{E}) = 0 \quad \forall\, \mathbf{x} \in S_2 \tag{20b}$$

As a result, the weak form is ended up with

$$c(\mathbf{E},\mathbf{v}) = jk_0\langle\mathbf{n}\times\mathbf{v}, 2\mathbf{n}\times\mathbf{E}^{\mathbf{I}}\rangle_{S_1} \tag{21}$$

where
$c(\mathbf{E},\mathbf{v}) = a(\mathbf{E},\mathbf{v}) + jk_0\langle\mathbf{n}\times\mathbf{v},\mathbf{n}\times\mathbf{E}\rangle_{S_1} + jk_0\langle\mathbf{n}\times\mathbf{v},\mathbf{n}\times\mathbf{E}\rangle_{S_2}$.

3.2. The objective function and its sensitivity analysis

In order to seek an optimal topology for a desired permeability of metamaterials, the simplest choice of the objective function J is the least square of the difference between the target μ^* and the imaginary part of the effective $\mathrm{Im}(\mu_{eff})$, read as

$$J = 1/2(\mathrm{Im}(\mu_{eff}) - \mu^*)^2 \tag{22}$$

One of the most important issues in metamaterial topology optimization is how to derive the sensitivity of the objective functional with respect to a perturbation induced

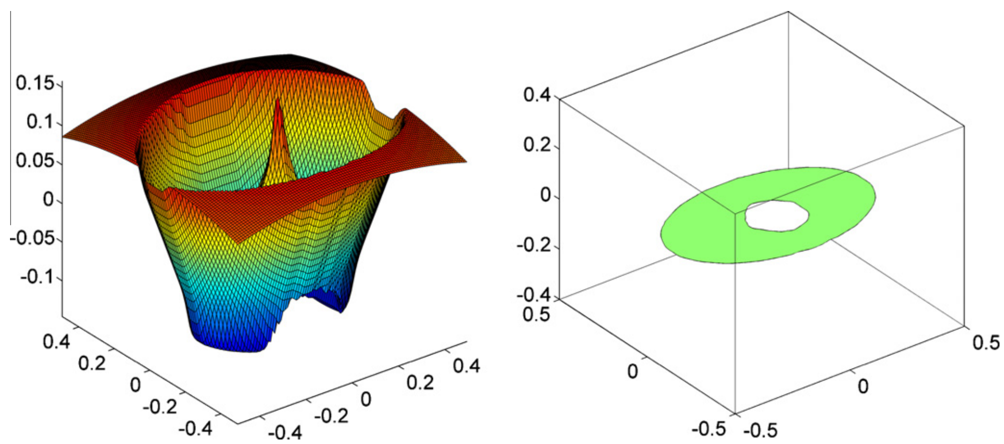

Fig. 3. The level-set function (left) and its zero-level contour (right).

by the variation of metal material. By associating the governing wave equation with the objective function, we obtained a Lagrangian functional, as

$$L(t,\mathbf{E},\mathbf{w}) = 1/2\big(\mathrm{Im}(\mu_{eff}) - \mu^*\big)^2 + \mathrm{Re}\Big(\big\langle \chi_\mu \nabla\times\nabla\times\mathbf{E},\mathbf{w}\big\rangle_{\Omega_0} - \big\langle \big(k_0^2\chi_\varepsilon - j\omega\mu_0\chi_\sigma\big)\mathbf{E},\mathbf{w}\big\rangle_{\Omega_0}\Big) \tag{23}$$

where the Lagrangian multiplier **w** is the solution to the adjoint system of the waveguide equation, which will be discussed later. In a common procedure of the level-set-based electromagnetic problem [31–33], only the real part (Re) of the waveguide equation is taken into account in the Lagrangian functional. In fact, the consideration of its imaginary part (Im) has the same effect on the optimization.

The dependence of the time (t) in Eq. (23) is implicitly expressed by the level-set function φ in the characteristic functions. According to the second vector Green's theorem $\langle \mathbf{a},\nabla\times\nabla\times\mathbf{b}\rangle_{\Omega_0} = \langle \mathbf{b},\nabla\times\nabla\times\mathbf{a}\rangle_{\Omega_0} - \langle \mathbf{a}\times\nabla\times\mathbf{b} - \mathbf{b}\times\nabla\times\mathbf{a},\mathbf{n}\rangle_{\partial\Omega_0}$ and the boundary conditions in Eq. (20), the second term of the Lagrangian functional becomes

$$\begin{aligned}\big\langle \chi_\mu\nabla\times\nabla\times\mathbf{E},\mathbf{w}\big\rangle_{\Omega_0} &= \langle \chi_\mu\mathbf{E},\nabla\times\nabla\times\mathbf{w}\rangle_{\Omega_0} + \langle \chi_\mu\mathbf{E}\times\nabla\times\mathbf{w},\mathbf{n}\rangle_{\partial\Omega_0} - \langle \chi_\mu\mathbf{w}\times\nabla\times\mathbf{E},\mathbf{n}\rangle_{\partial\Omega_0}\\ &= \langle \chi_\mu\mathbf{E},\nabla\times\nabla\times\mathbf{w}\rangle_{\Omega_0} - \langle \mathbf{E},\mathbf{n}\times\nabla\times\mathbf{w}\rangle_{S_1\cup S_2} + \langle \mathbf{w},\mathbf{n}\times\nabla\times\mathbf{E}\rangle_{\partial\Omega_0}\\ &= \langle \chi_\mu\mathbf{E},\nabla\times\nabla\times\mathbf{w}\rangle_{\Omega_0} - \langle \mathbf{E},\mathbf{n}\times\nabla\times\mathbf{w}\rangle_{S_1\cup S_2} + jk_0\langle \mathbf{n}\times\mathbf{w},\mathbf{n}\times\mathbf{E} - 2\mathbf{n}\times\mathbf{E}^{\mathbf{I}}\rangle_{S_1} + jk_0\langle \mathbf{n}\times\mathbf{w},\mathbf{n}\times\mathbf{E}\rangle_{S_2}\end{aligned} \tag{24}$$

Since Eq. (24) is applicable to both the real and imaginary parts, the real/imaginary symbol is not expressed explicitly.

Mathematically, the original objective is formulated as the min–max of the Lagrangian functional, read as [40]

$$J = \min_{\mathbf{E}}\max_{\mathbf{w}} L \tag{25}$$

The optimality of the Lagrangian functional is located at a saddle point, at which the partial derivatives of the Lagrangian functional with respect to **E** and **w** should be zero, as

$$\frac{\partial L}{\partial \mathrm{Re}(\mathbf{E})} = \frac{\partial L}{\partial \mathrm{Im}(\mathbf{E})} = \frac{\partial L}{\partial \mathrm{Re}(\mathbf{w})} = \frac{\partial L}{\partial \mathrm{Im}(\mathbf{w})} = 0 \tag{26}$$

Plugging Eq. (24) into the Lagrangian function and differentiating it with respect to the real part of the electric field and multiplying it by the test function **v**, we obtained

$$\begin{aligned}&\Big\langle \frac{\partial L}{\partial \mathrm{Re}(\mathbf{E})}\mathbf{I},\mathbf{v}\Big\rangle_{\Omega_0} = 0\\ &\Rightarrow \langle \chi_\mu\nabla\times\mathbf{v},\nabla\times\mathbf{w}\rangle_{\Omega_0} - \langle \mathbf{v}\times\nabla\times\mathbf{w},\mathbf{n}\rangle_{S_1\cup S_2} - \big\langle \big(k_0^2\chi_\varepsilon - j\omega\mu_0\chi_\sigma\big)\mathbf{v},\mathbf{w}\big\rangle_{\Omega_0}\\ &\quad - \langle \mathbf{v},\mathbf{n}\times\nabla\times\mathbf{w}\rangle_{S_1\cup S_2} + jk_0\langle \mathbf{n}\times\mathbf{w},\mathbf{n}\times\mathbf{v}\rangle_{S_1\cup S_2}\\ &= -\Big\langle \mathbf{v},\frac{(\mu_{eff}-\mu^*)\partial\mu_{eff}}{\partial \mathrm{Re}(E)}\Big\rangle_{\Omega_0} \Rightarrow c(\mathbf{v},\mathbf{w})\\ &= -\mathbf{v}\cdot\Big(\big(\mu_{eff}-\mu^*\big)\frac{\partial\mu_{eff}}{\partial \mathrm{Re}(E)}\mathbf{I}\Big)\end{aligned} \tag{27}$$

where **I** is the unit vector. Eq. (27) is named as the adjoint system of the vector waveguide equation.

Cuer and Zolésio [41] stated that the Eulerian derivative of the Lagrangian function with respect to time t equals to its partial derivative, specifically

$$dL/dt = \partial L(t,\mathbf{E},\mathbf{w})/\partial t \tag{28}$$

Since the dependence of this partial derivative on t is uniquely associated with the level-set φ in the characteristic functions, we obtained

$$dL/dt = \mathrm{Re}\Big(\langle (1-1/\mu_r)H'(\varphi)\nabla\times\mathbf{E},\nabla\times\mathbf{w}\rangle_{\Omega_0} - \big\langle \big(k_0^2(1-\varepsilon_r) + j\omega\mu_0\sigma\big)H'(\varphi)\mathbf{E},\mathbf{w}\big\rangle_{\Omega_0}\Big) \tag{29}$$

where the Dirac function is given as $H'(\varphi) = (\partial H(\varphi)/\partial\varphi)(\partial\varphi/\partial t) = \delta(\varphi)\partial\varphi/\partial t$. Since $\mu_r = \varepsilon_r = 1$ in Ω_0/Ω, the active domain in Eq. (29) is confined to Ω, as

$$dL/dt = \mathrm{Re}(\langle (1-1/\mu_r)H'(\varphi)\nabla\times\mathbf{E},\nabla\times\mathbf{w}\rangle_\Omega - \langle (k_0^2(1-\varepsilon_r) + j\omega\mu_0\sigma)H'(\varphi)\mathbf{E},\mathbf{w}\rangle_\Omega) \tag{30}$$

From the HJ equation, we thus obtained $\partial\varphi/\partial t = -V_n\|\nabla\varphi\|$. Furthermore, the relation of volume integral to surface integral can be expressed as

$$\int_\Omega V_n\delta(\varphi)\|\nabla\varphi\|d\Omega = \int_\Gamma V_n\, d\Omega \tag{31}$$

Plugging the HJ equation and Eq. (31) into Eq. (30), we obtain

$$dL/dt = -\mathrm{Re}(\langle (1-1/\mu_r)V_n\nabla\times\mathbf{E},\nabla\times\mathbf{w}\rangle_\Gamma - \langle (k_0^2(1-\varepsilon_r) + j\omega\mu_0\sigma)V_n\mathbf{E},\mathbf{w}\rangle_\Gamma) \tag{32}$$

Since the metal material considered is gold with nearly perfect conductivity, either electric or the adjoint field cannot sustain inside the metal or its boundaries. Thus the last term in Eq. (32) can be dropped, making the Eulerian derivative of the Lagrangian functional read as

$$\frac{dL}{dt} = -\mathrm{Re}(\langle (1-1/\mu_r)V_n\nabla\times\mathbf{E},\nabla\times\mathbf{w}\rangle_\Gamma) \tag{33}$$

When the normal velocity V_n in the level-set model is given as

$$V_n = \mathrm{Re}(\langle \nabla\times\mathbf{E},\nabla\times\mathbf{w}\rangle_\Gamma) \tag{34}$$

the Eulerian derivative becomes

$$dL/dt = -(1 - 1/\mu_r)\mathrm{Re}(\langle \nabla \times \mathbf{E}, \nabla \times \mathbf{w}\rangle)_\Gamma^2 \leqslant 0 \tag{35}$$

Eq. (35) is non-positive because $\mu_r > 1$ for all conducting materials. Thus it can drive the objective function towards an optimum at which the effective permeability approaches to the target.

3.3. Numerical implementation

Since the weak form of the adjoint system in Eq. (27) has the same left-hand side as that of the governing equations in Eq. (21), we only considered its right side herein. By using the chain rule, its right-hand side becomes

$$-\left\langle \mathbf{v}, \frac{(\mu_{eff} - \mu^*)\partial\mu_{eff}}{\partial\mathrm{Re}(E)}\right\rangle_{\Omega_0} = -(\mu_{eff} - \mu^*) \times \left(\mathbf{v} \cdot \left(\frac{\partial\mu_{eff}}{\partial S_{11}}\frac{\partial S_{11}}{\partial\mathrm{Re}(E)} + \frac{\partial\mu_{eff}}{\partial S_{21}}\frac{\partial S_{21}}{\partial\mathrm{Re}(E)}\right)\mathbf{I}\right) \tag{36}$$

Thus the adjoint system can be separated into the following two sub-adjoint equations as

$$c(\mathbf{v}, \mathbf{w}_1) = -\frac{2\exp^{-jk_0z_1}(\mu_{eff} - \mu^*)}{a^2E_0}\frac{\partial\mu_{eff}}{\partial S_{11}}\langle \mathbf{n} \times \mathbf{v}, \mathbf{n} \times \mathbf{y}\rangle_{S_1} \tag{37}$$

$$c(\mathbf{v}, \mathbf{w}_2) = -\frac{2\exp^{jk_0z_2}(\mu_{eff} - \mu^*)}{a^2E_0}\frac{\partial\mu_{eff}}{\partial S_{21}}\langle \mathbf{n} \times \mathbf{v}, \mathbf{n} \times \mathbf{y}\rangle_{S_2} \tag{38}$$

The solution to the adjoint equation equals the summation of the solutions to these two sub-adjoint equations due to their linear relationship, namely $\mathbf{w} = \mathbf{w}_1 + \mathbf{w}_2$. Compared with the right-hand side of the weak form of the governing equation $jk_0\langle \mathbf{n} \times \mathbf{v}, 2\mathbf{n} \times \mathbf{E}^{\mathbf{I}}\rangle_{S_1}$, the right-hand side of Eq. (37) is linearly proportional to that in Eq. (21). Thus, we concluded that the first sub-adjoint system is self-adjoint and its solution equals

$$\mathbf{w}_1 = -\frac{2\exp^{-jk_0z_1}(\mu_{eff} - \mu^*)}{a^2E_0}\frac{\partial\mu_{eff}}{\partial S_{11}}\frac{1}{2jk_0E_0\exp^{-jk_0z_1}}\mathrm{E} = \frac{(\mu_{eff} - \mu^*)}{k_0a^2E_0^2}\frac{\partial\mu_{eff}}{\partial S_{11}}j\mathrm{E} \tag{39}$$

By swapping the position of the incident (S_1) and receiving surfaces (S_2) in the simulation model, the incident wave and the right-hand side of the weak form become $\mathbf{E}^{\mathbf{I}} = E_0\mathbf{y}\exp^{jk_0z_2}$ and $-jk_0\langle \mathbf{n} \times \mathbf{v}, 2\mathbf{n} \times \mathbf{E}^{\mathbf{I}}\rangle_{S_2}$, respectively. An electric field $\mathbf{G}$ can be obtained and the solution to the second sub-adjoint equation equals

$$\mathbf{w}_2 = \frac{2\exp^{jk_0z_2}(\mu_{eff} - \mu^*)}{a^2E_0}\frac{\partial\mu_{eff}}{\partial S_{21}}\frac{1}{2jk_0E_0\exp^{jk_0z2}}\mathbf{G} = -\frac{(\mu_{eff} - \mu^*)}{k_0a^2E_0^2}\frac{\partial\mu_{eff}}{\partial S_{21}}j\mathbf{G} \tag{40}$$

One of the most popular approaches to the solution of the vector wave equation has been the FDTD method [35], which is a finite difference algorithm with stable and fast convergence. As FDTD is a well-established technique, it is not discussed here. Interested readers can consult relevant references.

4. Demonstrative examples

In addition to the objective function defined in Eq. (22), where a target is expected to be attained, the minimal effective permeability will be sought in some examples below. A volume constraint is used herein to avoid multiple solutions, make the different stages of design more comparable, and prevent large volume fraction fluctuations that may lead to numerical instabilities. In this paper, the bi-section algorithm [23] is used to maintain a nearly constant metal volume. In addition to this technique, the Newtown's method was reported to be effective for such a constraint in level-set model [22].

Since typical metamaterials have been usually singly symmetrical, a geometrical constraint is applied to keep the structure symmetric with respect to the horizontal axis. The finest mesh adopted in the following examples is $ny \times nz = 64 \times 64$, which is considered adequate to capture the major geometrical features of the structures. A finer mesh like $ny \times nz = 128 \times 128$ was tested but it increased the computational cost drastically without evident improvement of the optimization results.

4.1. The objective function with targeted effective permeability

The mesh size for the first example is $ny \times nz = 64 \times 64$ and the constraint of the volume fraction for metal (gold) region is $V_0 = 0.1140$. We first attempted to make the imaginary part of the effective permeability attain the target of $\mathrm{Im}(\mu_{eff}) = -0.07$ at the frequency of $f = 0.62$ THz.

As shown in Fig. 4, this example starts from a number of randomly distributed circles with vertically symmetric constraint at iteration $m = 0$. Because some circles are overlapping, the connected parts form a truss-like structure in the first snapshot of Fig. 4 (the metal region is colored in green in the base cell). The snapshots show that the level-set model handles the topological changes rather smoothly with the mergence of the circles and quickly shapes a distinct metal object at the early stage ($m = 0$–12). Correspondingly, the reduction in the objective function is quite evident in this stage (Fig. 5a), especially when topological change takes place. For example, when the left bar breaks at iteration $m = 22$ (Fig. 4), the objective function drops quickly from 4.45×10^{-4} to 1.38×10^{-4} (Fig. 5a).

In this example, the shape optimization dominates the subsequent evolution ($m = 22$–40) except some minor topological variation (e.g. the disappearance of two small holes inside the two arms from $m = 21$ to $m = 28$ in Fig. 4). It is noted that the design only takes 30 iterations to converge to an optimum. Nevertheless, we should bear in mind that the convergent speed largely depends on a

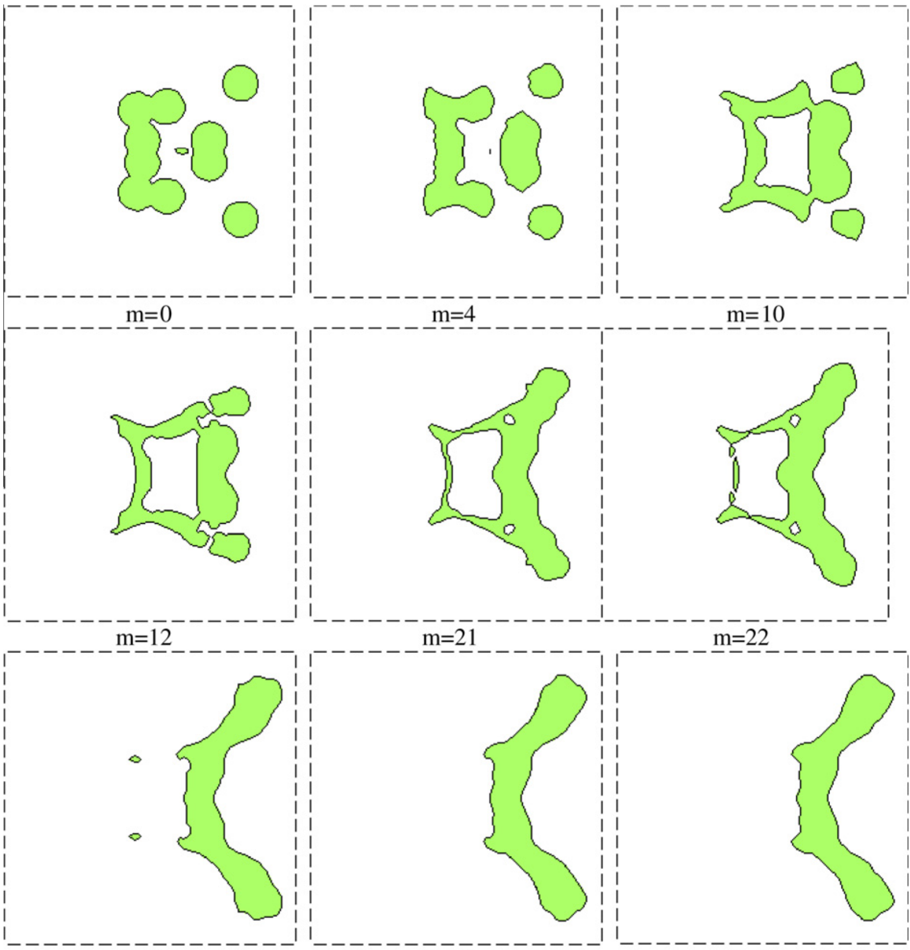

Fig. 4. The snapshots of the metal object in different iteration steps (Example 1).

number of factors, such as the initial structure, band width 2η of the approximation to the Heaviside function in Eq. (17) and the parameters of level-set method. Overall, all the examples in this paper demonstrate that the optimization can be converged fairly well.

Fig. 6 shows $\mathrm{Im}(\mu_{eff})$ in a spectrum of frequencies in different iteration steps, which exhibit that the negative peak of $\mathrm{Im}(\mu_{eff})$ drifts from right to left with the attained $\mathrm{Im}(\mu_{eff})$ (denoted by black dots) approaching to its target closely (red pentagram) at given frequency ($f = 0.62$ THz). In addition to the above-mentioned phenomenon, it is noted in Fig. 6 that the minimal value of $\mathrm{Im}(\mu_{eff})$ in different steps increases a bit as the optimization progresses. To have a clearer view of the decrease of $\mathrm{Im}(\mu_{eff})$ at $f = 0.62$ THz,

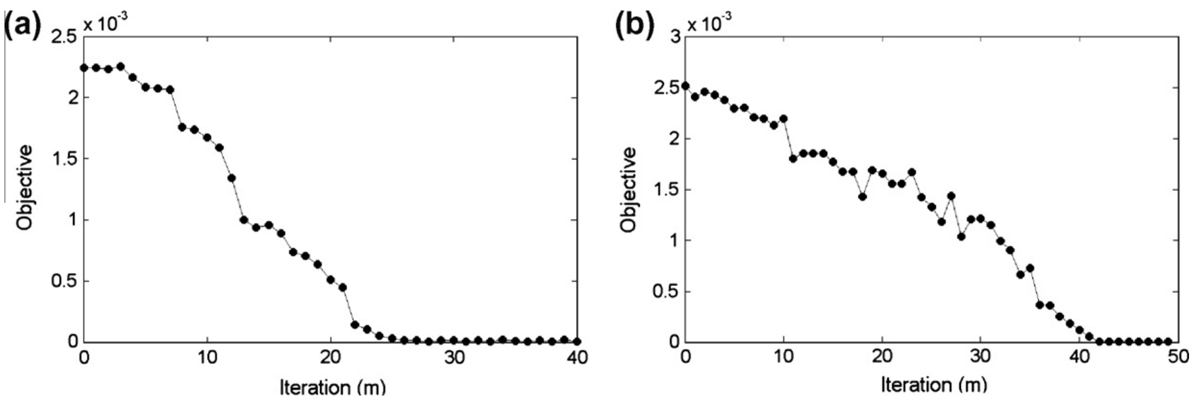

Fig. 5. The convergences of the objective function for: (a) Example 1 and (b) Example 2.

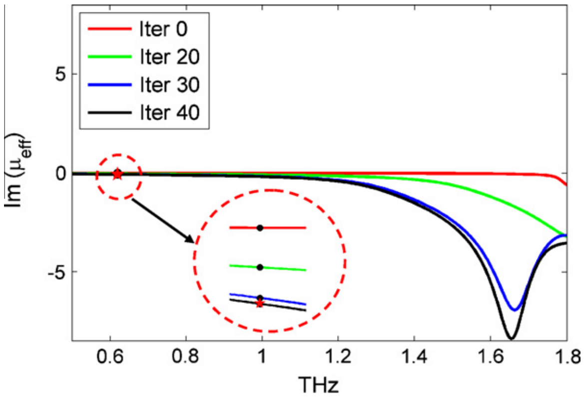

Fig. 6. Im(μ_{eff}) in a spectrum of frequencies and at given frequency (Example 1).

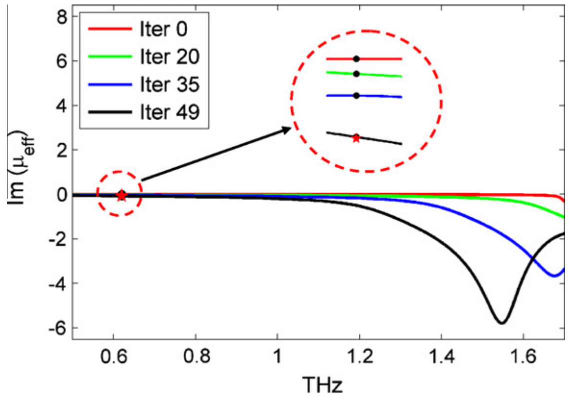

Fig. 8. Im(μ_{eff}) in a spectrum of frequencies and at given frequency (Example 2).

the part in the circled dashed zone is enlarged in a larger insert view in Fig. 6.

Example 2 starts from a circle centrally located in the base cell and confined to a volume fraction of $V_0 = 0.25$ at $m = 0$ (Fig. 7). It is discretized into a mesh of $ny \times nz = 32 \times 32$. We also attempted to make Im(μ_{eff}) attain –0.07 at $f = 0.62$ THz.

Fig. 7 shows the snapshots for this example. It is seen that the evolution presents a shape optimization as it is not easy for the level-set method to create new holes. Nevertheless, it is noted that for some special initial designs with multiple holes or separated parts, such as Example 1, topology optimization can be triggered and handled during the evolution. In this example, the structure evolves

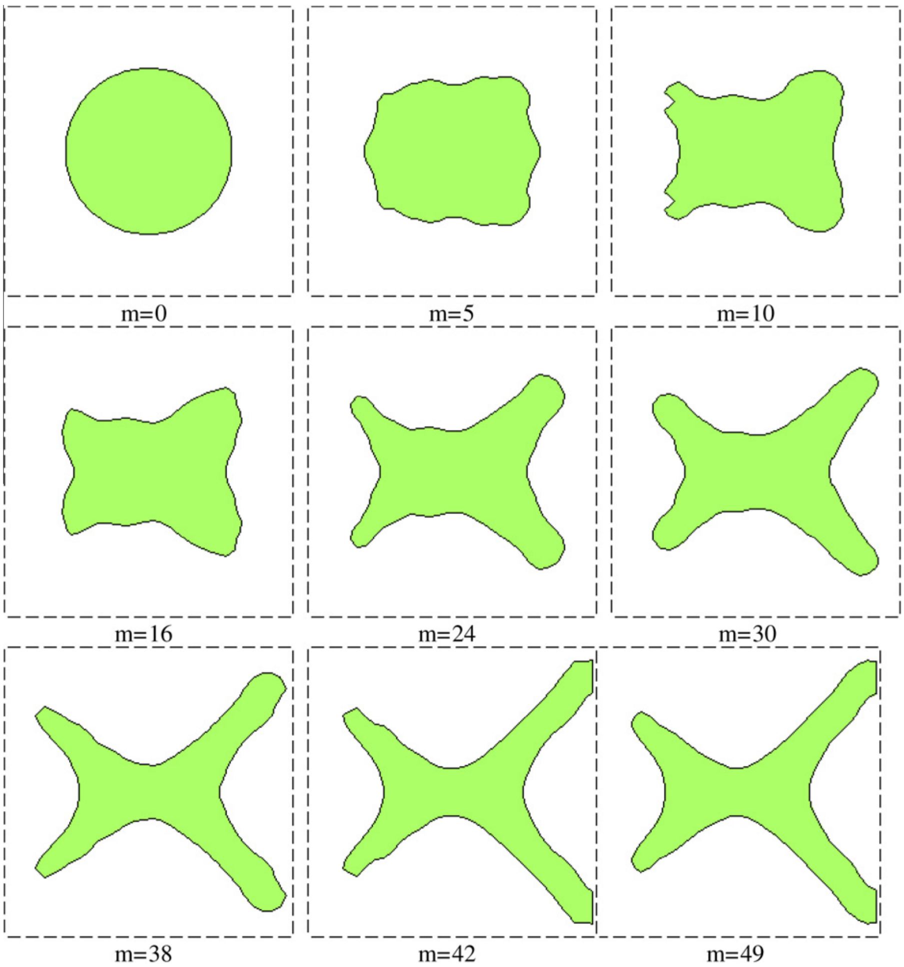

Fig. 7. The snapshots of the metal object in different iteration steps m (Example 2).

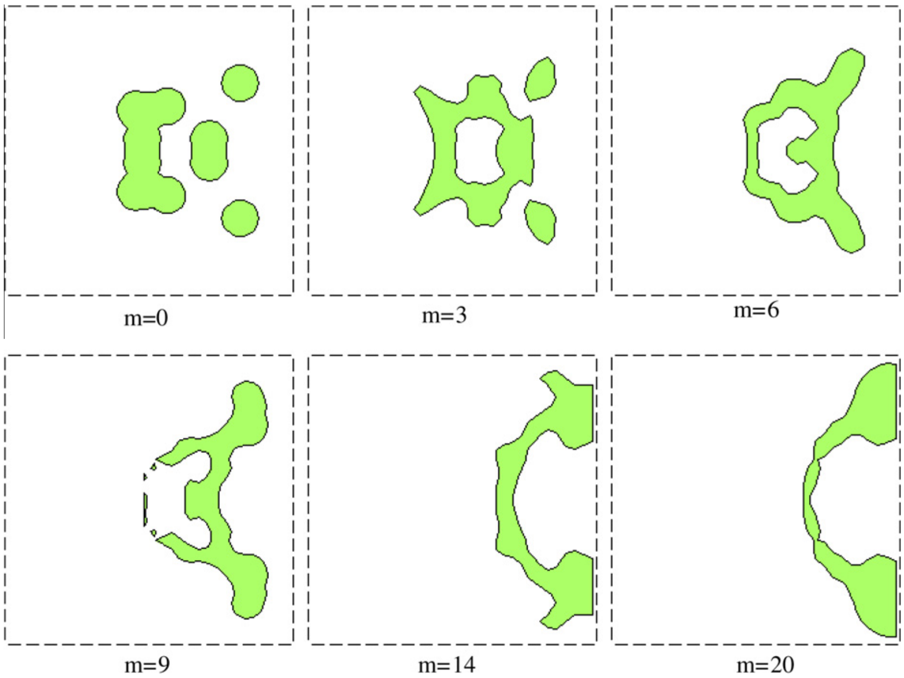

Fig. 9. The snapshots of the metal object in different iteration steps m (Example 3).

from a circle to a rectangular shape with dents in the middle of the four edges in the early stage ($m = 0$–16). As the optimization goes on, these four dents become deeper and wider while those four corners extend longer and longer ($m = 16$–49), gradually forming an X-shaped object ($m = 30$). It is noted that the right corners extend themselves much further along their diagonal directions, continuously from iteration $m = 30$ to $m = 49$; and finally form an elegant scissor-like structure ($m = 49$).

From the value of $\mathrm{Im}(\mu_{eff})$ at a spectrum of frequencies in Fig. 8, we noted that the initial circular solid does not have any negative $\mathrm{Im}(\mu_{eff})$ over a spectrum ranging from $f = 0.5$ THz to $f = 1.7$ THz. After the optimization, $\mathrm{Im}(\mu_{eff})$ drops to the negative territory over this spectrum and attains a negative value as low as $\mathrm{Im}(\mu_{eff}) = -6$ at $f = 1.56$ THz. The enlarged insert (circled in red[1] dashed line) in Fig. 8 clearly shows that $\mathrm{Im}(\mu_{eff})$ drops during the optimization and its final value attains the target (red pentagram) precisely. The convergence history for this example is illustrated in Fig. 5b, which shows a quick and continuous decrease in the objective function.

4.2. *The objective function targeted for minimal effective permeability*

In addition to the above-mentioned objective function in terms of the difference between the effective and target permeability, the level-set-based optimization method can be also applicable to other forms of objective functions. In this section, $\mathrm{Im}(\mu_{eff})$ will be used as a cost function:

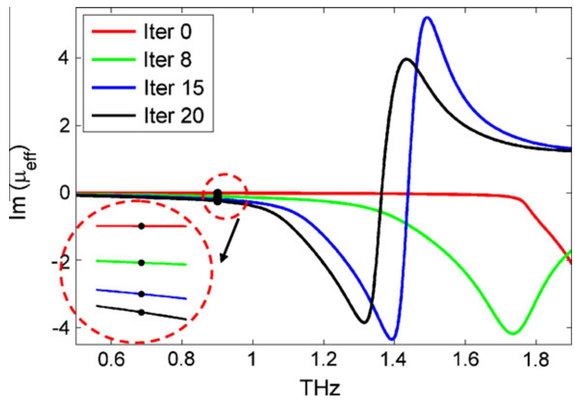

Fig. 10. $\mathrm{Im}(\mu_{eff})$ in a spectrum of frequencies and at given frequency (Example 3).

$$J = \mathrm{Im}(\mu_{eff}) \tag{41}$$

The following two examples aim to minimize $\mathrm{Im}(\mu_{eff})$ at a specific frequency $f = 0.90$ THz with different mesh sizes.

Example 3 (Fig. 9) starts from a vertical symmetry structure generated from several randomly distributed circles. The volume constraint of $V_0 = 0.1182$ and a mesh size of $ny \times nz = 32 \times 32$ are adopted here. The snapshots in Fig. 9 show that the circles merge rather quickly ($m = 3$) and form a structure with one hole and two antennas ($m = 6$). Then the hole breaks on the left-hand side ($m = 9$) and finally shapes the structure into a well-known U-shaped structure ($m = 20$). Interestingly, it shows that some parts of the final structure ($m = 20$) appear relatively thin, which induces high current flow density and resonance that is in good agreement with our recent findings in [25]. However, these thinner parts are quite easy to break

[1] For interpretation of color in Figs. 1–4 and 6–14, the reader is referred to the web version of this article.

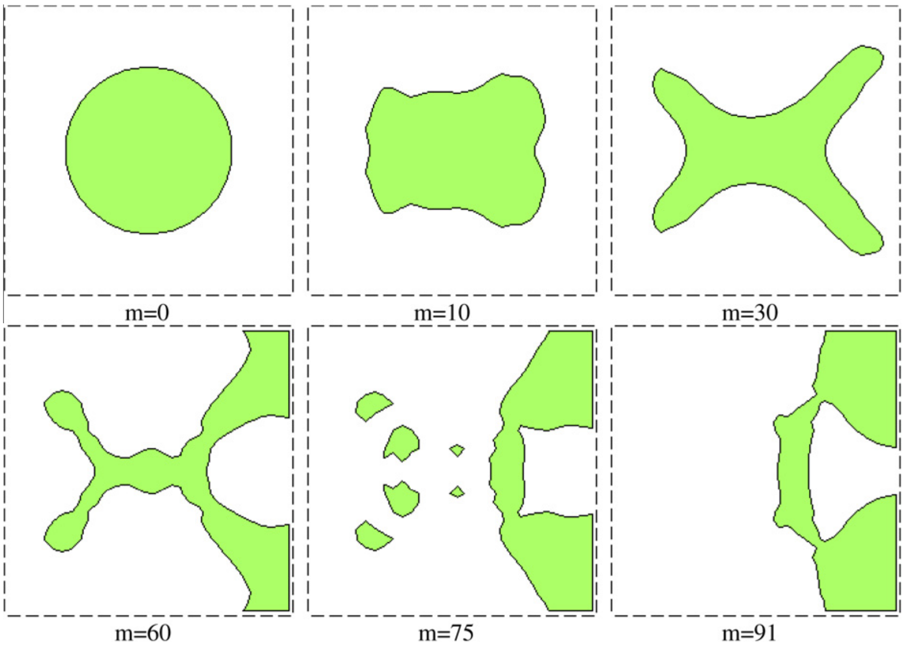

Fig. 11. The snapshots of the metal objects in different iteration steps m (Example 3).

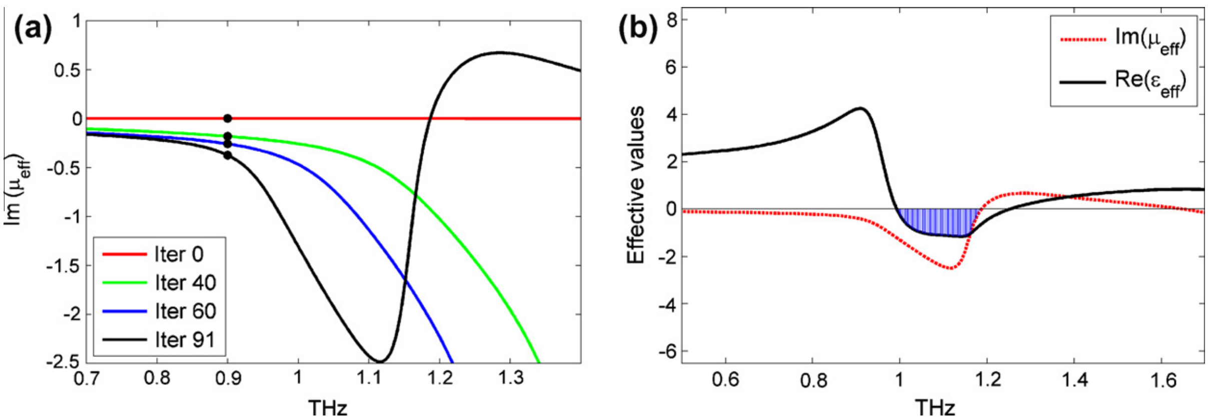

Fig. 12. The effective properties in a spectrum of frequencies for: (a) the intermediate structures and (b) final structure (Example 4).

if the mesh size is not sufficiently fine. Nevertheless, the optimization procedure can reconnect the broken parts in the subsequent iterations, indicating that the optimization reaches a fluctuant convergence.

The zoomed-in part in Fig. 10 clearly shows that Im(μ_{eff}) changes from −0.008 to −0.2411 at the specific frequency $f = 0.90$ within the 20 iterations. In the mean time, Im(μ_{eff}) falls into the negative territory over a spectrum range of $f = 0.8$–1.8 THz and the negative peaks of Im(μ_{eff}) drift from right to left during the optimization.

In Example 4 (Fig. 11), the design objective and parameters are the same as those in Example 3 except for the volume fraction ($V_0 = 0.25$) and initial structure (a circle). Since the optimization starts from the same circular structure as in Example 2, they come with a similar shape change in the beginning of the optimization ($m = 0$–30). Nevertheless, the topological variation takes place in the late stage of Example 4, making the left scissors-like the structure finally smashed out ($m = 30$–75). Whereas its right part gradually evolves to a SRR-like structure with a non-uniform thickness. Evidently, Im(μ_{eff}) drops from +0.001 to −0.3748 (Fig. 12a) during the optimization. In the mean time, the real part of the effective permittivity Re(ε_{eff}) falls into negative territory as well, rendering the final structure ($m = 91$) a negative refractive index in the frequency region as highlighted in blue in Fig. 12b.

Example 5 (Fig. 13) aims to minimize Im(μ_{eff}) at a frequency of $f = 0.62$ THz but with a finer mesh of $ny \times nz = 64 \times 64$. The optimization starts from several randomly distributed circles with a vertical symmetry and some overlapping ($V_0 = 0.0977$). The snapshots in Fig. 13 indicate that the central circles are reshaped into an I-shaped structure in the first 20 iterations, while the random circles on the boundaries gradually diminish ($m = 0$–30)

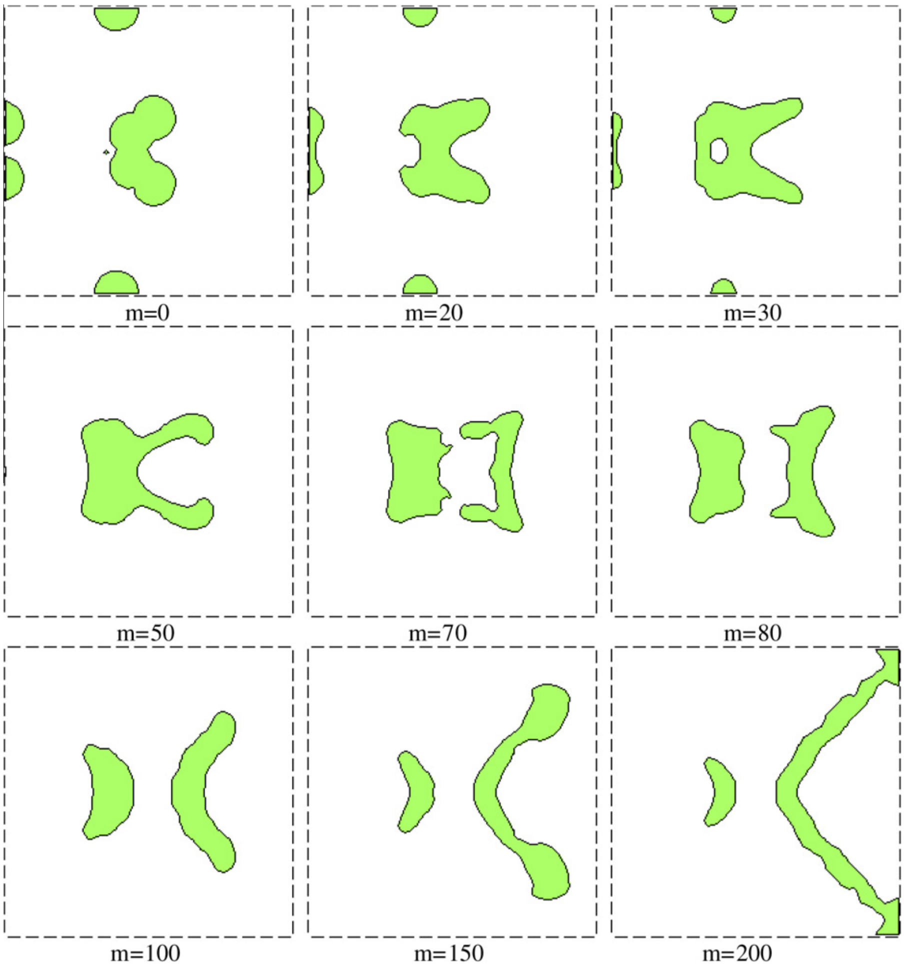

Fig. 13. The snapshots of the metal object in different iteration steps m (Example 5).

and finally disappear after iteration $m = 30$. The left ends of the I-shaped object enclose in iterations $m = 20$–30, forming a small hole in the solid region. With the disappearance of this hole, an elegant forceps-like structure is developed ($m = 50$). But such a structure seems unstable and quickly breaks into two separate parts ($m = 70$): the left one shrinks gradually but does not disappear completely; the right part grows up along the diagonal directions and finally its two ends reach the bottom/top-right corners ($m = 200$). Note that the right part of the structure is actually a V-shaped object, which is fairly similar to the commonly used U-shaped metamaterial structure.

Fig. 14a clearly shows $\mathrm{Im}(\mu_{eff})$ changes from 0.0068 to -0.1082 consistently during the optimization. Again, since both $\mathrm{Im}(\mu_{eff})$ and $\mathrm{Re}(\varepsilon_{eff})$ fall into the negative territory, the structure has a negative refractive index over a range of

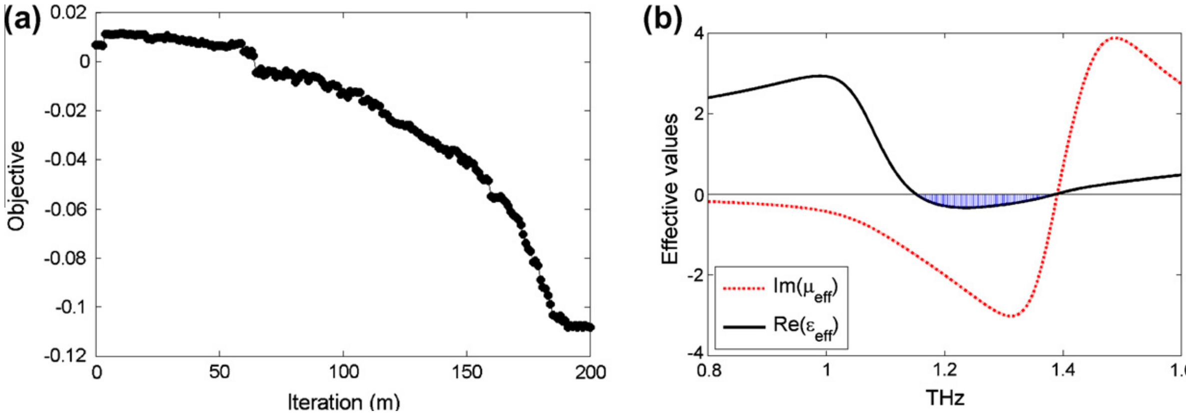

Fig. 14. The effective properties in a spectrum of frequencies for: (a) the intermediate structures and (b) final structure (Example 5).

frequencies (1.2–1.4 THz), as highlighted in blue region in Fig. 14b.

Similar to the structures generated by the SIMP method in Ref. [14], the level-set approach presented here also yields a U-like topology when taking into account the effective permeability in the objective functions. It is noted that, different from typical structural optimization, the resonance frequency and effective permeability in the electromagnetic metamaterials can be rather sensitive to a topological variation. The SIMP model requires some special filters and/or hybrid algorithm to avoid the resultant gray areas [14]. The level-set design, on the other hand, presents sharp topological boundaries without ambiguousness. The corresponding convergences of objectives in these level-set examples are fairly stable even with some significant change in the topologies.

5. Concluding remarks

This paper attempts to develop a topology optimization method for metamaterial design within a level-set framework. Specifically, the free space/solid (metal) interface is implicitly represented by the zero-level contour of a higher-dimensional scalar level-set function. Two different objective functions are tested at specific frequency: (1) the least square of the difference between the effective and target permeabilities, and (2) the effective permeability itself. As only the electric field is related to the effective permeability, the vector wave equation is used as the governing equation in this study.

To make the Eulerian derivative of the Lagrangian function, namely a summation of the objective function and the governing equation, dissipative with respect to time, the normal velocity of the Hamilton–Jacobi equation is derived. With such normal velocity, the free space/metal interface gradually evolves toward an optimum. Since both the governing and adjoint equations are solved by the FDTD method, the design domain can be discretized with a reasonably fine mesh to better capture the detailed geometrical and physical features of the metamaterial. The numerical examples demonstrate the effectiveness of the proposed level-set topology optimization approach for metamaterial design. Several novel structures are obtained and their effective permeabilities do attain the specified targets or the minimum at the given frequency specified.

Acknowledgement

This study was supported under Australian Research Council (ARC) (project numbers DP110104698 and LP0776938).

References

[1] Veselago VG. Sov Phys USPEKI 1968;10:509.
[2] Saadoun MMI, Engheta N. Microwave Opt Technol Lett 1992;5:184.
[3] Lagarkov AN, Semenenko VN, Chistyaev VA, Ryabov DE, Tretyakov SA, Simovski CR. Electromagnetics 1997;17:213.
[4] Pendry JB, Holden AJ, Robbins DJ, Stewart WJ. IEEE Trans Microwave Theory Tech 1999;47:2075.
[5] Smith DR, Padilla WJ, Vier DC, Nemat-Nasser SC, Schultz S. Phys Rev Lett 2000;84:4184.
[6] Pendry JB, Schurig D, Smith DR. Science 2006;312:1780.
[7] Pendry JB. Phys Rev Lett 2000;85:3966.
[8] Chen HS, Ran LX, Huangfu JT, Zhang XM, Chen KS. Phys Rev E 2004;70:057605.
[9] Liu N, Guo HC, Fu LW, Kaiser S, Schweizer H, Giessen H. Nat Mater 2008;7:31.
[10] Padilla WJ, Aronsson MT, Highstrete C, Lee M, Taylor AJ, Averitt RD. Phys Rev B 2007;75(1/4):041102.
[11] Chen PY, Chen CH, Wang H, Tsai JH, Ni WX. Opt Express 2008;16:12806.
[12] Rozvany GIN, Zhou M, Birker T. Struct Optim 1992;4:250.
[13] Bendsøe MP. Struct Optim 1990;1:193.
[14] Diaz AR, Sigmund O. Struct Multidiscip Optim 2010;41:163.
[15] Haug EJ, Choi KK, Komkov V. Design sensitivity analysis of structural systems. Orlando (FL): Academic Press; 1986.
[16] Svanberg K. Int J Numer Methods Eng 1987;24:359.
[17] Osher S, Sethian JA. J Comput Phys 1988;78:12.
[18] Sussman M, Smereka P, Osher S. J Comput Phys 1994;114:146.
[19] Sethian JA, Wiegmann A. J Comput Phys 2000;163:489.
[20] Wang MY, Wang XM, Guo DM. Comput Methods Appl Mech Eng 2003;192:227.
[21] Allaire G, Jouve F, Toader AM. J Comput Phys 2004;194:363.
[22] Jung Y, Chu KT, Torquato S. J Comput Phys 2007;223:711.
[23] Zhou SW, Li Q. J Comput Phys 2008;227:10178.
[24] He L, Kindermann S, Sini M. J Comput Phys 2009;228:717.
[25] Zhou SW, Li W, Sun GY, Li Q. Opt Express 2010;18:6693.
[26] Zhou SW, Li W, Li Q. J Comput Phys 2010;229:6915.
[27] Quek SS, Xiang Y, Zhang YW, Srolovitz DJ, Lu C. Acta Mater 2007;54:2371.
[28] Xiang Y, Cheng LT, Srolovitz DJ, Weinan E. Acta Mater 2003;18:5499.
[29] Challis VJ, Guest JK. Int J Numer Methods Eng 2009;79:1284.
[30] Harrington RF. Field computation by the moment methods. New York: IEEE Press; 1993.
[31] Santosa F. ESAIM: Control Optim Calculus Variations 1996;1:17.
[32] Dorn O, Lesselier D. Inverse Problems 2006;22:R67.
[33] Burger M, Osher SJ. Euro J Appl Math 2005;16:263.
[34] Bendsøe MP, Sigmund O. Topology optimisation: theory, methods, and applications. Berlin: Springer Verlag; 2003.
[35] Yee K. IEEE Trans Antennas Propagation 1966;14:302.
[36] Jin JM. Finite element method in electromagnetics. New York: John Wiley; 1993.
[37] The CST reference guide: CST Inc.; 2008.
[38] Lubkowski G, Schuhmann R, Weiland T. Microwave Opt Technol Lett 2006;49:285.
[39] Smith DR, Vier DC, TKoschny T, Soukoulis CM. Phys Rev E 2005;71:036617.
[40] Ramananjaona C, Lambert M, Lesselier D, Zolésio J-P. Inverse Problems 2001;17:1087.
[41] Cuer M, Zolésio JP. Control Lett 1988;11:151.